3D Multi-fluid MHD Simulation of the Early Time Behavior of an Artificial Plasma Cloud in the Bottom Side Ionosphere

Daniel M. Ober[1], Trevor S. Crawford[2], James V. Eccles[3], Jeffrey M. Holmes[1]

[1]Space Vehicles Directorate, Air Force Research Laboratory, Kirtland Air Force Base, Albuquerque, New Mexico, USA.

[2]Earth Resources Technology, Inc. (ERT), Laurel, Maryland, USA.

[3]Space Dynamics Lab, Utah State University, Utah, USA.

Corresponding author: Daniel Ober (rvborgmailbox@us.af.mil)

Key Points:

- An oxygen ion enhancement develops in the cloud center that evolves into a depletion with enhancements on opposite field-aligned sides.
- The barium and oxygen ions rotate about the central axis of the cloud due to the velocity difference term in the ion momentum equation.
- The ion cloud alternates rotation direction and the magnetic field twist radiates along the magnetic field line as a shear Alfvén wave.

Abstract

A multi-fluid magnetohydrodynamic model has been developed to investigate artificial clouds in the lower ionosphere. The model is based on the five-moment approximation of the fluid equations with separate continuity and momentum equations for each species. The model can have multiple neutral and ion species, background and cloud designation of species, and multiple chemical reactions between species. The model is used to simulate a barium cloud initiated in the bottom side ionosphere. The neutral barium cloud is observed to expand radially with a spherical density distribution. The barium ion cloud, produced by ionization of the neutral barium cloud, expands mostly along the magnetic field lines. Both the barium and oxygen ions are observed to rotate about the magnetic field. A diamagnetic cavity develops quickly and then collapses within the 10s model period. Initially there is an oxygen ion density enhancement in the center of the cloud that later evolves into a depletion with enhancements on opposite field-aligned sides of the depletion. The direction of the ion rotation about the magnetic field alternates with time. The associated magnetic field twist propagates away from the cloud along the field line as a shear Alfvén wave. This last result, previously unreported, results from the additional physics included in the multi-fluid formulation of the fluid equations.

Plain Language Summary

A numerical fluid model was developed that is used to investigate the early time expansion of an artificially-generated cloud in the upper atmosphere. In the model results, disturbances in the background ionosphere and thermosphere are observed due to the expanding cloud. The expanding cloud is observed to rotate about the magnetic field due to the different forces acting on it. Electromagnetic waves, produced by the rotating cloud, are observed radiating along the magnetic field line away from the artificial cloud.

1 Introduction

The evolution and dynamics of artificially created plasma clouds are rich with a variety of interesting plasma physics that has made them the subject of investigation for many decades [Davis, 1979, Haerendal, 2019]. Observations include radial expansion of the neutral cloud, field-aligned expansion of the ion cloud, development of a diamagnetic cavity and collapse, snowplowed background ions, "skidding" of the ion cloud, electron heating, and small or large scale structuring of the ions described as striations, flutes, sheets, and/or surface waves [*Rosenberg*, 1971; Lühr et al., 1986; *Bernhardt et al.*, 1987; Lühr et al ., 1988; *Bernhardt*, 1992; Huba et al., 1992; Blaunstein et al., 1993; *Delamere et al.*, 1996; *Szuszczewicz et al.*, 1996]. For artificial clouds produced in the bottom-side ionosphere, affects have been observed in the underlying E-region as well [*Stoffregen*, 1970], and surprisingly some artificial clouds have been observed as much as 10 hours after the initial release [*Milinevsky et al.*, 1993].

Numerous models have been developed over the decades using a variety of approaches (e.g. fluid models, particle-in-cell models, hybrid models, chemistry models, and empirical models) for investigating the dynamics and stability of artificial plasma clouds [*Ma and Schunk*, 1991; *Ma and Schunk*, 1993, *Ma and Schunk,* 1994; *Winske*, 1998; *Xie et al.*, 2014; *Bernhardt et al.*, 2017; *Holmes et al.*, 2017, *Pedersen et al.*, 2017; *Zhang et al.*, 2019]. Here we are primarily interested in three-dimensional fluid models.

A three-dimensional time-dependent numerical model was developed by *Ma and Schunk* [1991] that solved the single fluid continuity and momentum equations for multiple ion and neutral background and cloud species. Divergence-free current closure is assumed when solving for a potential electric field, and the background magnetic field was assumed static. Collisions between species are included as well as a chemistry source term for the photoionization of the neutral release cloud. A drift-diffusion approximation is used when solving the ion momentum equation where the ion velocity in the inertial term is replaced with a zero-order approximation.

Ma and Schunk [1993], hereafter referred to as MS93, used this model to study the early time evolution of an artificial barium clouds in the ionosphere. For an ion cloud with no directional velocity in a uniform background, it was found that: 1) the neutral barium cloud expanded radially in all directions, 2) the barium ion cloud, produced from photoionization of the neutral barium cloud, expanded primarily in the field-aligned direction producing a spheroidal

shaped ion cloud, particularly evident in the central region of the cloud, 3) a density depletion developed in the background oxygen ions with density enhancements on opposite field-aligned sides of the depletion, and 4) both the barium and oxygen ions circulated in the same direction, but with different angular velocities, around the central field-aligned axis of the cloud. The oxygen ion density enhancements were attributed to the electrostatic snowplow affect. The circulation of the barium and oxygen ions was attributed to a combination of E cross B and diamagnetic drift. This model was later extended to include realistic E and F region density profiles [*Ma and Schunk*, 1994]. A similar model was later used to study the long time evolution of a cesium ion cloud in the ionosphere [*Zhang et al.*, 2019].

A three-dimensional two-species single-fluid magnetohydrodynamic (MHD) model was used to investigate the Combined Release and Radiation Effects Satellite (CRRES) mission G2 barium release in the magnetosphere [*Xie et al.*, 2014]. Their model solved the continuity, momentum, and energy equations for the time-dependent evolution of the ions and magnetic field. The neutral barium cloud was described by a Gaussian density profile that expanded with time. Results are presented for a barium cloud released with an initial directional velocity transverse to the magnetic field. The model results showed expansion of the neutral and ion clouds, a fast Alfvén wave propagating outward in all directions, the expansion and collapse of a diamagnetic cavity, and a density depletion in the hydrogen ion background with density enhancements on opposite field-aligned sides of the central depletion.

The development of magnetic cavities and surface structures on an expanding cloud have also been investigated using three-dimensional MHD, Hall MHD, and particle codes [*Winske et al.*, 2019].

In this paper we use a multi-fluid MHD model to study the early-time dynamics of an expanding barium cloud in the lower ionosphere/thermosphere. The difference between multi-species and multi-fluid models is that in the multi-fluid approach the different species are treated as separate fluids that can move relative to each other, and the presence of a “velocity difference” term in the ion momentum equation that takes into account affects due to the relative motion of each ion species [*Ledvina et al.*, 2008]. In the multi-fluid approach diffusion occurs naturally as a result of each species ability to move relative to each other. The results reported

here describe a simulation of a barium cloud in the bottom-side ionosphere, with initial conditions that closely match those used by MS93.

This paper is organized into 4 sections. In section 2 we describe the basic equations used in the model and presuppositions. Section 3 covers model initialization and numerical techniques. Section 4 provides a discussion of model outputs with a conclusion in section 5.

2 Model Description

The Special Transport and Chemistry (STC) model has been developed to investigate the dynamics of artificial plasma clouds. Our model is a time-dependent three-dimensional model based on the five-moment equations [*Schunk*, 1977] for each neutral and ion species. It is assumed that each species can be effectively described by a drifting Maxwell-Boltzmann distribution. The STC formulation is capable of handling multiple chemical species and numerous chemical reactions between those species. For the purpose of comparing with MS93, the energy equation is not solved, and constant temperature has been assumed.

2.1 The Transport Equations

The continuity and momentum transport equations for the neutral species are

$$\frac{\partial n_\alpha}{\partial t} + \nabla \cdot \left(n_\alpha \vec{V}_\alpha\right) = S_{n_\alpha} \tag{1}$$

$$\frac{\partial \left(\rho_\alpha \vec{V}_\alpha\right)}{\partial t} + \nabla \cdot \left(\rho_\alpha \vec{V}_\alpha \vec{V}_\alpha\right) = -\nabla p_\alpha + \sum_{\beta=i,n} \rho_\alpha \nu_{\alpha\beta}\left(\vec{V}_\beta - \vec{V}_\alpha\right) + S_{\rho_\alpha \vec{V}_\alpha} \tag{2}$$

where n_α, ρ_α, $\vec{V}_\alpha$, and p_α, are the number density, mass density, velocity, and pressure of species α, $\nu_{\alpha\beta}$ is the momentum exchange collision frequency between species α and β, and S is a source term due to chemistry [*Eccles and Raitt*, 1992]. The summation in the momentum exchange collision term is over all species, charged and neutral. The force terms on the right-hand-side of the momentum equation are the pressure gradient force, momentum exchange, and the chemistry source term.

131 The continuity and momentum transport equations for the ion species are

$$\frac{\partial n_\alpha}{\partial t} + \nabla \cdot \left(n_\alpha \vec{V}_\alpha\right) = S_{n_\alpha} \tag{3}$$

$$\begin{aligned}\frac{\partial\left(\rho_i \vec{V}_i\right)}{\partial t} + \nabla \cdot \left(\rho_i \vec{V}_i \vec{V}_i\right) \\ = -\nabla p_i - \frac{q_i n_i}{e n_e} \nabla p_e + q_i n_i \left(\vec{V}_i - \vec{V}_{ions}\right) \times \vec{B} + \frac{q_i n_i}{e n_e} \vec{J} \times \vec{B} \\ + \sum_{\beta=i,n} \rho_i \nu_{i\beta} \left(\vec{V}_\beta - \vec{V}_i\right) + S_{\rho_i \vec{V}_i}\end{aligned} \tag{4}$$

132 with

$$\vec{V}_{ions} = \frac{1}{e n_e} \sum_{\beta=i} q_\beta n_\beta \vec{V}_\beta \tag{5}$$

133 where q_α, e, $\vec{E}$, and $\vec{B}$ are the ion species charge, electron charge magnitude, electric field, and
134 magnetic field, and $\vec{V}_{ions}$ is the charge-averaged ion velocity. The force terms on the right-hand-
135 side of the ion momentum equation are the ion and electron pressure gradient force, a velocity
136 difference term, the ponder motive (or partial J cross B) force, momentum exchange, and a
137 chemistry source term. The velocity difference term is only nonzero when an ion species has a
138 flow velocity different from that of the charge-averaged ion velocity [*Winglee*, 2004; *Harnett*
139 *and Winglee*, 2005]. This term isn't present in the single fluid or multi-species approximation of
140 the fluid equations.

141 Faraday's Law completes the equation set with the induction equation for the evolution
142 of the magnetic field

$$\frac{\partial \vec{B}}{\partial t} + \nabla \cdot \left(\vec{B} \vec{V}_{ions}\right) = \nabla \cdot \left(\vec{V}_{ions} \vec{B}\right) - \nabla \times \frac{m_e \sum_{\beta=i,n} \nu_{e\beta}}{e^2 n_e} \vec{J} \tag{6}$$

143 Note that the magnetic field is tied to the charge-averaged ion velocity. Ampere's Law, ignoring
144 the displacement current, was used for the current density

$$\vec{J} = \frac{1}{\mu_0} \nabla \times \vec{B} \tag{7}$$

145 Charge neutrality is assumed ($n_i = n_e$) making it appropriate to ignore the displacement current
146 and is valid for spatial scales larger than the Debye length [*Ledvina et al.*, 2008]. Note, defining
147 the current density as the curl of $\vec{B}$ ensures the current is divergence free (i.e. current closure).

148 A modified Ohm's law equation has been substituted for the electric field, when deriving
149 the ion momentum equation and the induction equation, which was derived from the electron
150 momentum equation

$$\vec{E} = -\vec{V}_e \times \vec{B} - \frac{1}{en_e}\nabla p_e + \frac{1}{en_e}\sum_{\beta=i,n} \rho_e \nu_{e\beta}\left(\vec{V}_\beta - \vec{V}_e\right) \tag{8}$$

151 Using the electron drift velocity derived from the definition of the current density

$$\vec{V}_e = \frac{1}{en_e}\sum_{\beta=i} q_\beta n_\beta \vec{V}_\beta - \frac{1}{en_e}\vec{J} \tag{9}$$

152 in the ohm's law equation for the electric field results in

$$\vec{E} = -\frac{1}{en_e}\sum_{\beta=i} q_\beta n_\beta \vec{V}_\beta \times \vec{B} + \frac{1}{en_e}\vec{J} \times \vec{B} - \frac{1}{en_e\mu_0}\nabla p_e + \frac{m_e \sum_{\beta=i,n} \nu_{e\beta}}{e^2 n_e}\vec{J} \tag{10}$$

153 where the various terms on the right-hand-side of the equation are the V cross B term, the Hall
154 term, the ambipolar electric field term, and an ohmic resistive term. The Ohmic resistive term in
155 the Ohm's law relation was dropped when substituting for the electric field in the ion momentum
156 equation and both the hall and electron pressure gradient terms were dropped when substituting
157 for the electric field in the induction equation.

158

159 2.2 The Collision Frequencies

160 The momentum transfer collision frequencies are all calculated from theoretical
161 expressions appropriate for the five-moment approximation [*Schunk and Nagy*, 1980]. The
162 neutral-neutral (hard sphere) momentum transfer collision frequency between neutral species s
163 and t is

$$\nu_{st} = \frac{8}{3\sqrt{\pi}}\frac{n_t m_t}{m_s + m_t}\left(\frac{2k_B T_{st}}{\mu_{st}}\right)^{1/2} \pi(r_s + r_t)^2 \tag{11}$$

where k_B is Boltzman's constant and μ_{st} is the reduced mass defined as

$$\mu_{st} = \frac{m_s m_t}{m_s + m_t} \tag{12}$$

and T_{st} is the reduced temperature defined as

$$T_{st} = \frac{m_s T_t + m_t T_s}{m_s + m_t} \tag{13}$$

and r is the Van Der Waals radius. Values for the Van Der Waals radius used in the model calculations were taken from *Mantina et al.* [2013].

The ion-ion, ion-electron, electron-ion, and electron-electron (coulomb interaction) momentum transfer collision frequency between species *s* and *t* is

$$\nu_{st} = \frac{16\sqrt{\pi}}{3} \frac{n_t m_t}{m_s + m_t} \left(\frac{2 k_B T_{st}}{\mu_{st}} \right)^{-3/2} \frac{k_e^2 {e_s}^2 {e_t}^2}{\mu_{st}^2} ln\Lambda \tag{14}$$

where k_e is Coulomb's constant ($k_e = 1/4\pi\epsilon_0$ where ϵ_0 is the permittivity of free space) and $ln\Lambda$ is the Coulomb logarithm.

The non-resonant ion-neutral (Maxwell molecule interactions) momentum transfer collision frequency between ion species *i* and neutral species *n* is

$$\nu_{in} = 2.21\pi \frac{n_n m_n}{m_i + m_n} \left(\frac{\gamma_n k_e e^2}{\mu_{in}} \right)^{1/2} \tag{15}$$

where γ_n is the neutral gas polarizability. Since momentum is conserved, the momentum lost by one species has to be equal to the momentum gained by the other species, therefore

$$n_i m_i \nu_{in} = n_n m_n \nu_{ni} \tag{16}$$

2.3 Chemistry

For the chemical reaction of photo ionization of neutral barium, the reaction is

$$Ba + h\nu \rightarrow Ba^+ + e^- \tag{17}$$

Photo ionization results in the loss of neutral barium and the production of barium ions. The source terms for conservation of mass of Ba and Ba^+ are therefore

$$S_{n_{Ba}} = -kn_{Ba} \tag{18}$$

and

$$S_{n_{Ba^+}} = kn_{Ba} \tag{19}$$

where k is the photo ionization rate. It is assumed that the barium cloud is optically thin. This is a reasonable assumption for barium clouds with column densities less than $7.0 \cdot 10^{10}\ cm^{-2}$ [Stenbaek-Nielsen, 1989]. This condition is satisfied throughout the simulation.

Photo ionization also results in a loss of momentum from the neutral barium fluid and a source of momentum for the barium ion fluid. The source terms for conservation of momentum for Ba and Ba^+ are

$$S_{\rho_{Ba}\vec{V}_{Ba}} = -k\rho_{Ba}\vec{V}_{Ba} \tag{20}$$

and

$$S_{\rho_{Ba^+}\vec{V}_{Ba^+}} = k\rho_{Ba^+}\vec{V}_{Ba^+} \tag{21}$$

where it is assumed that the barium ions carry away all of the momentum of the parent neutral barium atoms.

2.4 Model Initialization and Numerical Approaches

This section introduces STC model initialization, coordinate system, and parameters associated with the initial plasma cloud. Numerical approaches are discussed as well.

2.4.1 Initialization

For this study, the model uses a Cartesian grid with dimensions of $300 \times 300 \times 888$, with the initial cloud centered at the origin. The starting physical size of each grid cell is $\Delta x = \Delta y = \Delta z = 150$ meters, and the computational domain is x from $-150\Delta x$ to $150\Delta x$, y from $-150\Delta y$ to $150\Delta y$, and z from $-444\Delta z$ to $444\Delta z$. As the cloud expands and approaches the boundary of the computational domain, a new larger grid is established. Each dimension of the new grid is double that of the original grid but with the same number of grid cells.

Therefore, 8 grid cells in the original grid map to one grid cell in the new grid, the new grid cell having the equivalent volume as the original 8 grid cells. All physical quantities are mapped and conserved onto the new spatially larger grid. In this simulation, this "re-gridding" process occurred 5 times. Free inflow/outflow boundary conditions (i.e. Neumann boundary conditions with no gradients across the boundary) are specified for all quantities with the boundary cells being set equal to the adjacent grid cell values.

Following MS93, the background consists of one thermosphere species of neutral oxygen, O, and one ionosphere species of oxygen ions, O^+. The O and O^+ densities are initialized across the entire domain as $1.0 \cdot 10^8\ cm^{-3}$ and $1.0 \cdot 10^6\ cm^{-3}$ respectively, with zero velocity. The background magnetic field is in the z direction, $\vec{B} = B_0\hat{z}$, with $B_0 = 3.0 \cdot 10^{-5}$ Tesla and is initialized uniformly across the grid. The artificial cloud consists of neutral barium, Ba. Only one chemical reaction is considered, the photo ionization of barium to produce barium ions, Ba^+. The barium photo ionization rate was $k = 0.04\ s^{-1}$.

The simulation begins at 0.1 seconds and finishes at 10 seconds. The initial ($t_0 = 0.1\ Sec$) density and velocity of the neutral barium cloud was taken to be the solution to the classical "steady state" diffusion at constant temperature [*Bernhardt*, 1979]. The solution to the 3-D diffusion equation for n and $\vec{V}$ is

$$n_{Ba}(x, y, z, t = t_0) = \frac{N_{Ba}}{(4\pi D_{Ba} t_0)^{3/2}} e^{-(x^2+y^2+z^2)/4D_{Ba}t_0} \tag{22}$$

$$\vec{V}_{Ba}(x, y, z, t = t_0) = \frac{\vec{r}}{2t_0} \tag{23}$$

where

$$D_{Ba} = \frac{kT_{Ba}}{m_{Ba}}\left(\frac{1}{\nu_{Ba,O} + \nu_{Ba,O^+}}\right) \tag{24}$$

and N_{Ba} is the total number of neutral barium atoms in the initial cloud. Equation 22 represents an initial Gaussian density profile. It is easily verified that equations 22 and 23 together are a solution to the continuity equation with no source terms. The total number of neutral barium atoms in the initial cloud was $N_{Ba} = 4.4 \cdot 10^{24}$ atoms.

The temperature of all species ($O, O^+, Ba,$ and Ba^+) was 1160 degrees Kelvin. The neutral barium and oxygen Van Der Waals radius [*Mantina et al.*, 2013] was $r_{Ba} = 2.68$ Å and $r_O = 1.52$ Å and the neutral gas polarizability [*Miller*, 2000] was $\gamma_{Ba} = 39.7$ and $\gamma_O = 0.802$.

With these values, the initial value for the barium diffusion coefficient D_{Ba} is $7.5 \cdot 10^6\ m^2/s$ which is slightly larger than the $1.75 \cdot 10^6\ m^2/s$ value used in the MS93 calculations. This means that for the simulation results reported here, the neutral barium cloud will expand faster than the neutral barium cloud in the MS93 results. In both MS93 and here the conditions are for a low beta plasma with both the electrons and ions frozen to the magnetic field (i.e. $\Omega_i > \nu_{in}$ and $\Omega_e > \nu_{en}$).

2.4.2 Numerical Techniques

The numerical framework used to solve the continuity, momentum, and induction equations is operator splitting [*MacNamara and Strang*, 2016]. This is a common technique that decouples PDE terms into simpler equations and allows the flexibility to incorporate different discretization methods to different parts of a PDE problem.

The flux corrected transport technique [*Boris and Book*, 1976] is applied to convective transport for mass and momentum (neutrals and ions only). The technique consists of computing a transport flux, diffusive flux, and an anti-diffusive flux such that the diffusive flux ensures stability and monotonicity, and the anti-diffusive flux removes excess diffusion where possible. Number densities below $1.0 \cdot 10^{-4}\ cm^{-3}$ are not tracked and are set to zero when they occur. To achieve second order accuracy in time, Strang splitting [*Strang*, 1968] is used to sub-step the solution forward in time. STC alternates the sub-stepping sequence between $L_x^{dt/2} L_y^{dt/2} L_z^{dt} L_y^{dt/2} L_x^{dt/2}$, $L_y^{dt/2} L_z^{dt/2} L_x^{dt} L_z^{dt/2} L_y^{dt/2}$, and $L_z^{dt/2} L_x^{dt/2} L_y^{dt} L_x^{dt/2} L_z^{dt/2}$. Numerical stability is attained by limiting the time step using the following

$$\Delta t \leq \frac{1}{2} \frac{\Delta d}{\max(|v_i| + \sqrt{c_{s,i}^2 + v_{A,i}^2})} \tag{25}$$

where Δd is the width of the grid cell, v_i is the species flow speed, c_s is the sound wave speed defined as

$$c_s = \sqrt{\frac{3k_B T_i}{m_i}} \tag{26}$$

and v_A is the Alfvén wave speed defined as

$$v_A = \frac{B_z}{\sqrt{\mu_0 \rho_i}} \tag{27}$$

The pressure gradient terms, velocity difference term, and the J cross B term in the momentum equation and the source term in the magnetic induction equation are all integrated using central difference Euler methods. The time step is defined as above.

The momentum exchange collision term in the momentum equation for neutrals and ions is solved using a first-order implicit scheme. The implicit scheme is stable for any step size, but with accuracy compromised for using a step size to large. Using the same step size that is used for the convection works well with no noticeable loss of accuracy in the momentum exchange due to collisions (i.e. momentum is conserved).

Chemistry, in general, will consist of a stiff set of N-coupled first-order non-linear differential equations. These equations can be solved using a semi-implicit midpoint rule [*Press et al.*, 1992]. Accuracy is achieved through an adaptive sub-stepping scheme. The Bulirsch-Stoer method [*Press et al.*, 1992] is used to extrapolate to an optimal solution using a sequence of increasingly smaller sub-steps. The chemistry solver was verified by comparing the results with those in Holmes et al. [2017].

The resistive term in the magnetic induction equation has the form of a parabolic equation. Due to the spatially varying diffusion term, a heuristic stability criterion is adopted where the diffusion term is computed at cell interfaces and the solution is approximated by sub-stepping a forward time center space differencing scheme [*Press et al.*, 1992].

3 Results

The 3D simulation results are presented in 2D slices through the origin in either the X-Y or X-Z planes at various times during the simulation, where the Z-axis is in the direction of the unperturbed B-field. In some of the plots, streamlines are used to show the direction, or arrows to show both direction and magnitude, of a vector field projected onto the plane shown. Half-width half-max is used throughout to describe the radius of the cloud, even when the shape of the cloud is not Gaussian.

The simulation begins at 0.1 seconds from a neutral barium cloud with a peak density of $1.5 \cdot 10^8\ cm^{-3}$ and a half-width half-max of $1.5\ km$. The initial barium cloud expands radially outward in all directions maintaining a spherical density distribution as shown in Figure 1a at 2 seconds in the simulation. The peak density of the barium cloud decreases with time as the cloud expands and as barium atoms are lost to photoionization. At 2 seconds the neutral barium cloud peak density was $1.25 \cdot 10^5\ cm^{-3}$ with a half-width half-max of $14.4\ km$. At 10 seconds (not shown) the neutral barium cloud peak density was $9.4 \cdot 10^2\ cm^{-3}$ with a half-width half-max of $57\ km$.

A barium ion cloud develops from photoionization of the neutral barium cloud. The barium ions expand outward primarily in the field-aligned direction producing a spheroidal shaped density distribution with major axis in the field-aligned direction as shown in Figure 1b. This is particularly apparent in the central denser part of the ion cloud. Photoionization continually produces additional barium ions with the spherical density distribution of the parent neutrals that

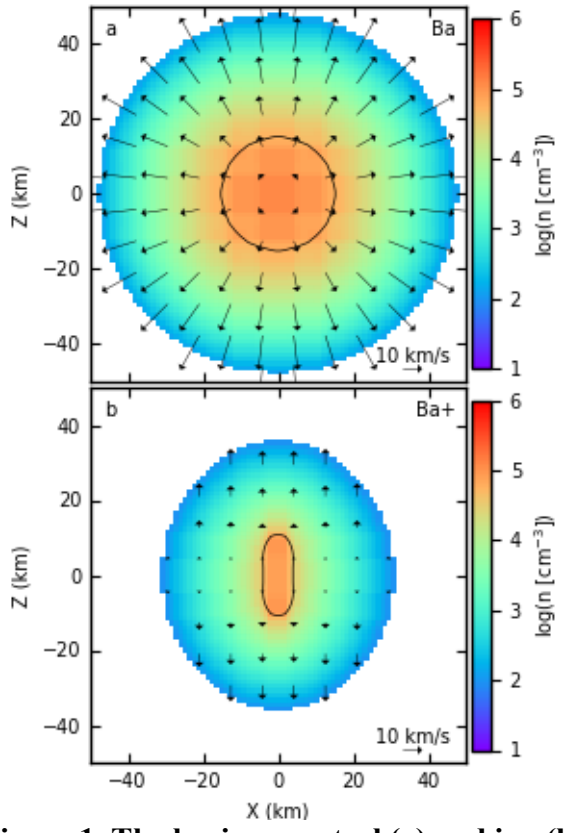

Figure 1. The barium neutral (a) and ion (b) number densities in the X-Z plane at 2.0 seconds. The arrows indicate the direction and magnitude of the flows in the X-Z plane. The black contour line indicates the size of the barium cloud at full-width half-max.

is most apparent in the outer portion of the ion cloud. At 2 seconds the barium ion cloud peak density was $8.3 \cdot 10^4\ cm^{-3}$ with a half-width half-max perpendicular to the magnetic field of $3.6\ km$ and parallel to the magnetic field of $12\ km$. At 10 seconds (not shown) the barium ion cloud had a half-width half-max of $9.6\ km$ and $24\ km$ perpendicular and parallel to the magnetic field, respectively, with a peak density of $1.5 \cdot 10^4\ cm^{-3}$ well below the background ionosphere oxygen ion density.

A spherical density depletion begins developing immediately in the background neutral oxygen (not shown) collocated with the central part of the barium cloud. At 2 seconds the neutral oxygen density depletion was 34.6 percent of the background value. The oxygen density depletion expands and deepens with time and persists until the end of the simulation at 10 seconds.

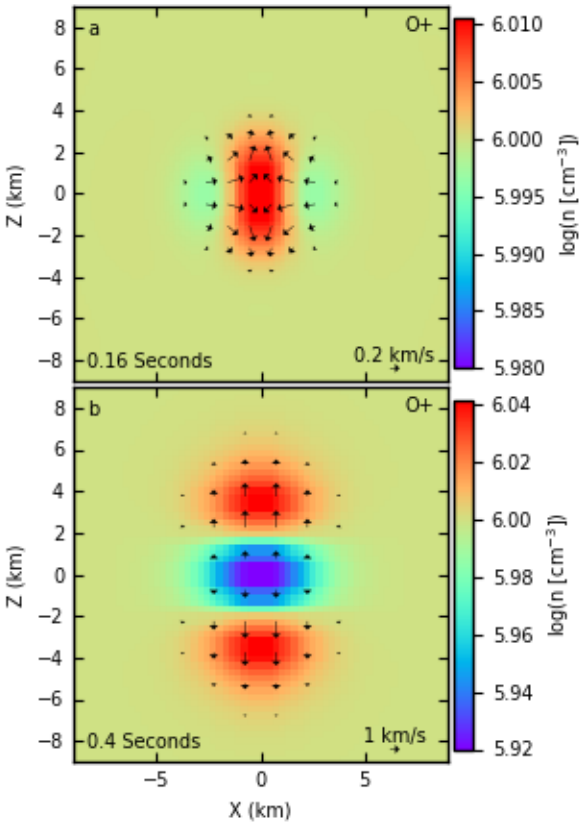

Figure 2. The oxygen ion number density in the X-Z plane at 0.16 (a) and 0.4 (b) seconds. The arrows indicate the direction and magnitude of the flows in the X-Z plane.

Initially an oxygen ion enhancement develops, shown in Figure 2a at 0.16 seconds, collocated with the central part of the barium ion cloud. The oxygen ion enhancement is surrounded by a torus-shaped oxygen ion density depletion. This later evolves into an oxygen ion density depletion collocated with the central part of the barium ion cloud with oxygen ion density enhancements on opposite field-aligned sides of the depletion, shown in Figure 2b at 0.4 seconds.

In the outer portion of the barium ion cloud, consisting mostly of recently ionized barium ions, the barium ion velocity perpendicular to the magnetic field is outward with a clock-wise rotation around the field-aligned (z-axis) of the cloud. Figure 3 plots the velocity magnitude and direction in the X-Y plane at the cloud center with B_Z out of the page. In the inner portion of the

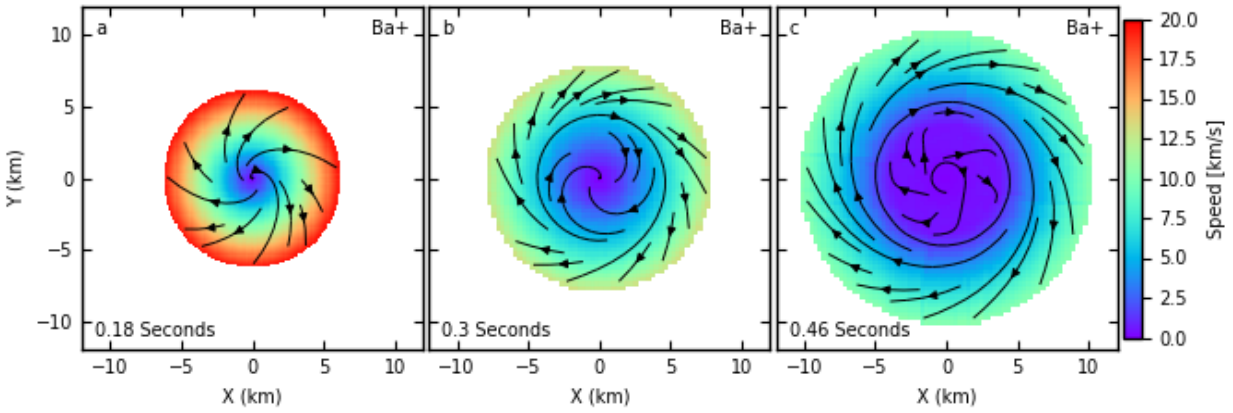

Figure 3. The barium ion flow velocity magnitude in the X-Y plane at 0.18 (a), 0.3 (b), and 0.46 (c) seconds. The streamlines indicate the direction of the flows in the X-Y plane.

barium ion cloud, the perpendicular velocity alternates between spiraling clockwise outward and clockwise inward as shown in Figure 3 at 0.18, 0.3, and 0.46 seconds. The barium ion flow parallel to the magnetic field is always outward, away from the midplane (z = 0) of the cloud.

The oxygen ion velocity, in the region overlapping the outer part of the barium ion cloud, alternates between outward and inward flow. In the region overlapping the inner part of the barium ion cloud the oxygen ion perpendicular velocity alternates between spiraling counter-clockwise inward and clockwise outward as shown in Figure 4 at 0.18, 0.3, and 0.46 seconds. The oxygen ion flows are much slower and in the opposite rotation direction compared to the barium ion flows near the cloud center. The oxygen ion flow parallel to the magnetic field is also always outward, away from the midplane of the barium ion cloud.

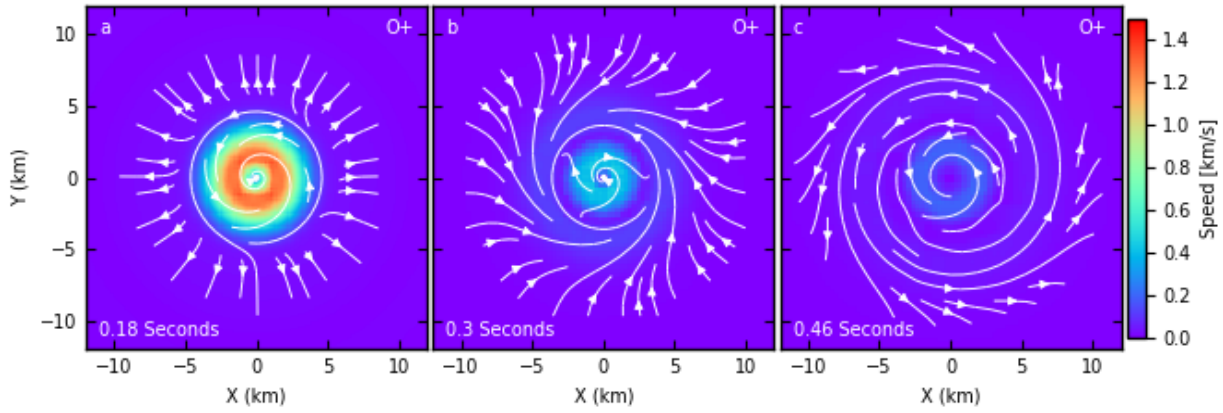

Figure 4. The oxygen ion flow velocity magnitude in the X-Y plane at 0.18 (a), 0.3 (b), and 0.46 (c) seconds. The streamlines indicate the direction of the flows in the X-Y plane.

A diamagnetic cavity develops, in the center of the barium ion cloud, with an associated diamagnetic current system that produces a dipole-like magnetic field perturbation around the diamagnetic cavity, shown in Figure 5 at 0.14 seconds. The reduction of the magnetic field in the diamagnetic cavity drops to 99.33 percent of the background value at its lowest value and completely recovered to background levels before the end of the simulation at 10 seconds. A compression wave with perturbations in the magnetic field and ion density was also observed (not shown) propagating away from the cloud in all directions at the start of the simulation.

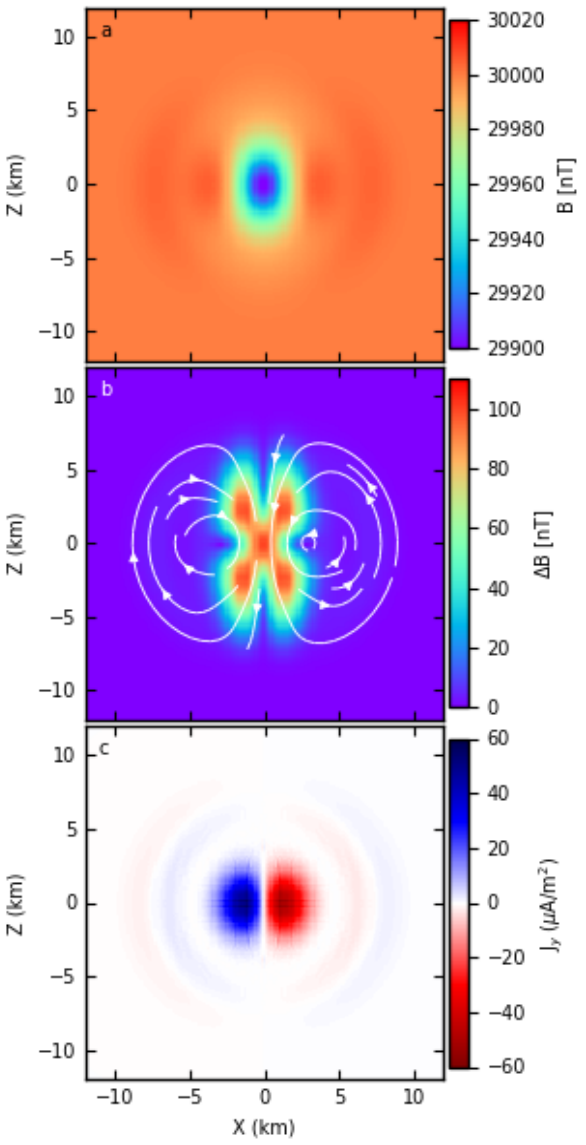

Figure 5. The magnitude of the total magnetic field (a) and perturbation magnetic field (b), and the y-component of the current density (c) in the X-Z plane at 0.14 seconds. The streamlines in panel b indicate the direction of the perturbation magnetic field in the X-Z plane.

Figure 6a shows the y-component of the charge-averaged ion velocity in the X-Z plane at 0.18 seconds. At this time the barium ions are flowing azimuthally rotating clockwise (Figure 3a) about the z-axis while the collocated oxygen ions are flowing counter-clockwise (Figure 4a). The charge-averaged ion velocity is counter-clockwise as shown in Figure 6a due to the higher oxygen ion number density compared to the barium ion number density in the center of the cloud. Collocated with the azimuthally flowing ions, the magnetic field is twisted in the counter-clockwise direction as shown in Figure 6b. Positive delta-By is into the page and negative delta-By is out of the page. A field-aligned current is also observed, Figure 6c, flowing towards the central region of the ion cloud. These field-aligned currents close by flowing outward perpendicular to the magnetic field near the

midplane of the cloud, and flowing away from the midplane along magnetic field lines near the outer regions of the cloud, followed by inward flow perpendicular to the magnetic field to complete the loop as indicated by the streamlines in Figure 6c.

The twisted magnetic field and corresponding field-aligned-current, propagates in the field-aligned direction away from the center of the cloud eventually extending well beyond the expanse of the barium ion cloud. After time, the rotation of the ions in the center of the cloud reverses direction. The twist in the magnetic field, and the direction of the field-aligned currents, reverses direction accordingly and then propagates away from the cloud in the field-aligned direction. This pattern repeats and a series of magnetic field twists and field-aligned currents are observed propagating away from the cloud in the field-aligned directions as shown in Figure 7 at times 0.3, 0.5, and 1 seconds. No perturbations in the magnetic field strength or in the background oxygen ion density are observed associated with the propagating waves beyond the expanse of the barium ion cloud. The ion rotation rate in the center of the cloud, and the associated magnetic field twist, diminishes in time with each reversal.

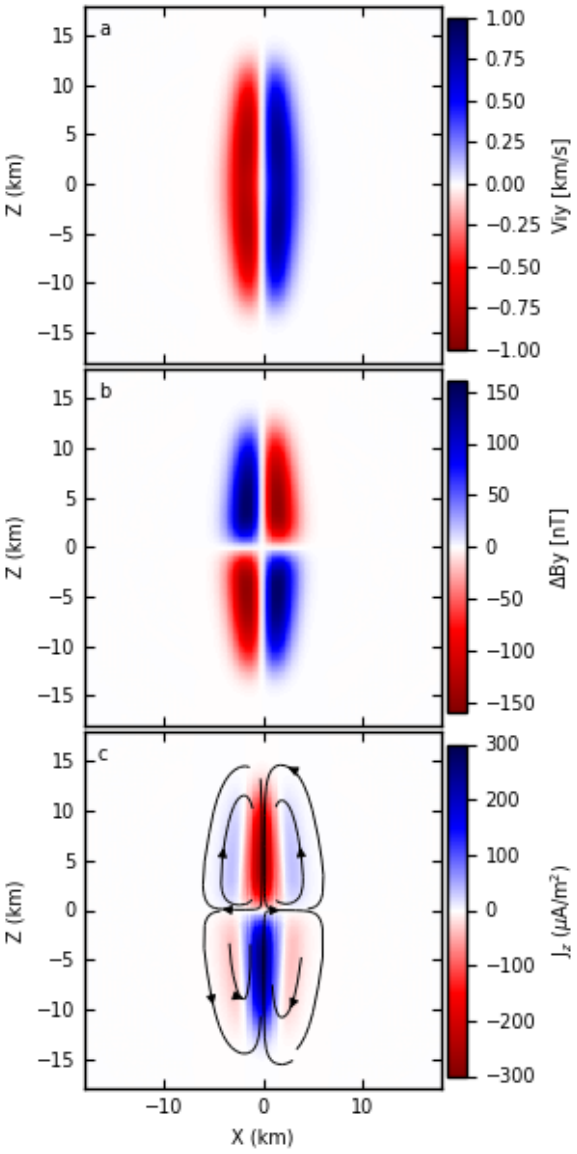

Figure 6. The y-component of the charge-averaged ion velocity (a), the y-component of the perturbation magnetic field (b), and the z-component of the current density (c) in the X-Z plane at 0.18 seconds. The streamlines in panel c indicate the direction of the current flow in the X-Z plane.

4 Discussion

The major differences between the MS93 model and the STC model are the way in which the electric and magnetic fields are calculated. In the MS93 model the electric field is calculated from an electrostatic potential derived using $\nabla \cdot \vec{J} = 0$ where $\vec{J}$ is calculated from the relative motion of the ions and electrons. The magnetic field is constant. In the STC model the electric field is calculated using an Ohm's law relation derived from the electron momentum equation. Ampere's law is used to calculate the currents from the curl of the magnetic field which implies $\nabla \cdot \vec{J} = 0$. The magnetic induction equation is used to calculate the magnetic field dynamics which leads to the development of the diamagnetic cavity and the Alfvén waves. The STC model extends the model results reported in MS93 with the inclusion of the induction electric field and the magnetodynamics.

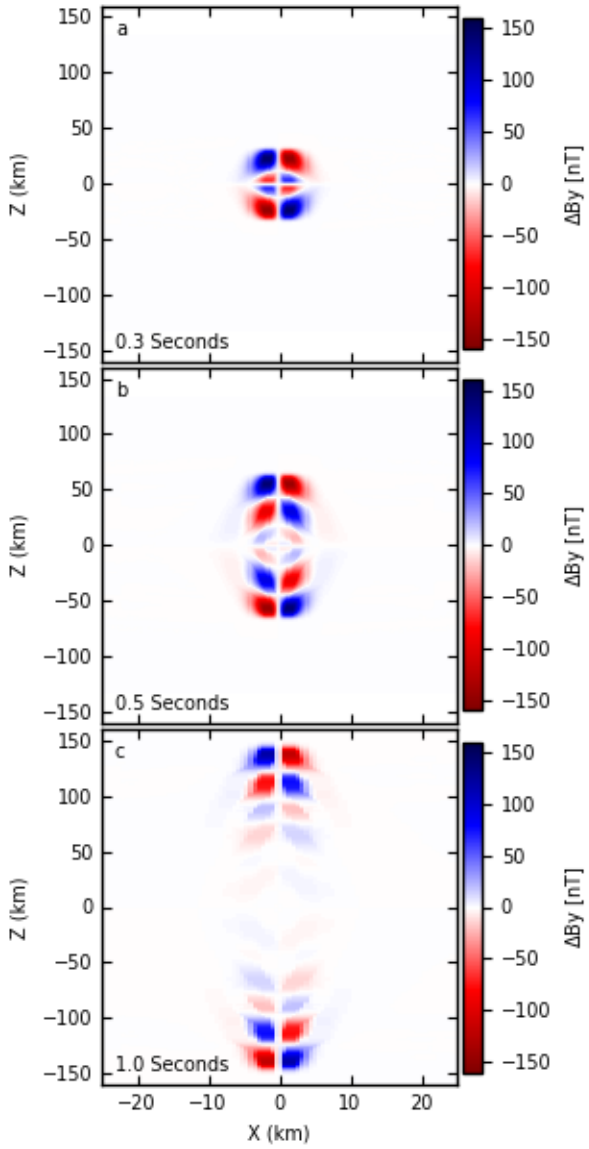

Figure 7. The y-component of the perturbation magnetic field in the X-Z plane at 0.3 (a), 0.5 (b), and 1.0 (c) seconds. The Z-axis has been compressed relative to the X-axis.

Several of the observed features in the STC model results are similar to what was observed in the MS93 results. The neutral barium cloud expanded radially in all directions. The barium ion cloud, produced from photoionization of the neutral barium cloud, expanded primarily in the field-aligned direction producing a spheroidal shaped ion cloud, particularly evident in the central region of the cloud. A density depletion developed (after an initial density enhancement) in the background oxygen ions with density enhancements on opposite field-aligned sides of the depletion. Both the barium and oxygen ions in the central region of the

cloud circulated around the central field-aligned axis of the cloud. The similarities between the MS93 and STC model results provides some verification of the STC model results. There are also several differences observed in the results of the two models, resulting from the inclusion of additional physics, including the development of the diamagnetic cavity, the alternating azimuthal flows of the ions in the central region of the cloud, and the Alfvén waves that propagate away from the cloud.

A diamagnetic cavity was observed to develop in the central region of the barium ion cloud. The diamagnetic cavity develops as a result of the radially outward flowing barium ions. The magnetic field can be thought of as moving outward with the charge-averaged ion velocity (Equation 6) producing the magnetic cavity. The resulting magnetic field gradients are responsible for producing the diamagnetic currents. The combination of the magnetic field and diamagnetic currents produces the J cross B force, or magnetic pressure and tension forces, that balances the ion pressure gradients and prevents the ion cloud from expanding perpendicular to the magnetic field. Diamagnetic cavities have been observed in the artificial ion clouds produced by AMPTE [Lühr et al., 1986; *Bernhardt et al.*, 1987; Lühr et al ., 1988] and CRESS [*Bernhardt*, 1992] although the observed diamagnetic cavities were all at much higher altitudes than the simulation results reported here. The size of the diamagnetic cavity that develops is limited by the kinetic energy of the ions producing it [*Winske et al.*, 2019; Haerendel 2019]. In the simulation results reported here, the reduction in the magnetic field at the center of the ion cloud is small and transient, disappearing quickly as the magnetic field diffuses back into the cloud due to the finite conductivity of the plasma (i.e. the resistive term in the magnetic induction equation).

Initially there is an oxygen ion density enhancement in the central region of the cloud driven by the partial J cross B force accelerating the oxygen ions perpendicular to the magnetic field towards the central region of the cloud. An oxygen ion density depletion is left in the wake of the inward moving ions producing the torus-shaped density depletion around the midplane of the cloud. The initial accumulation of oxygen ions in the center of the cloud produces pressure gradients that accelerate the ions outward along the magnetic field away from the midplane of the cloud. This field-aligned flow is further enhanced by both the ambipolar electric field and collisional coupling with the expanding cloud [Schunk and Szuszczewicz, 1991]. Ultimately the initial torus shaped density depletion in the midplane expands to fill the entire central region of

464 the cloud with density enhancements on opposite field-aligned sides of the depletion. Whether
465 the oxygen ion enhancements result primarily from kinetic snowplow or electrostatic snowplow
466 depends on the electron temperature and the relevant collision frequencies [*Schunk and*
467 *Szuszczewicz*, 1991].

468 The azimuthally flowing ions observed in both the cloud and background ions results
469 from the "velocity difference" term in the ion momentum equations. An identical simulation
470 was performed without the velocity difference term in the ion momentum equation. The results
471 were similar but without the azimuthal ion flows, the associated magnetic field line twist, or the
472 shear Alfvén wave that propagates away from the cloud. The velocity difference term creates a
473 force transverse to the flow when an ion specie velocity is different from the charge-averaged ion
474 velocity [Winglee, 2004]. Initially the barium ions are expanding radially outward in the
475 midplane of the cloud and the oxygen ions are stationary or moving slowly inwards toward the
476 center of the cloud. The charge-averaged ion velocity at this time is slowly outward. For the
477 outward flowing barium ions $\left(\vec{V}_i - \vec{V}_{ions}\right) \times \vec{B} > 0$ while for the inward flowing oxygen ions
478 $\left(\vec{V}_i - \vec{V}_{ions}\right) \times \vec{B} < 0$ causing the barium and oxygen ions to accelerate azimuthally in opposite
479 directions as shown in Figures 4a and 5a. The continued evolution of the ion flows in the cloud
480 are governed by the relative balance of the pressure gradients, the velocity difference term, the J
481 cross B force, and the collision forces between species. As the cloud expands and the cloud
482 expansion rate decreases the influence of the velocity difference term diminishes and the
483 magnitude of the ion azimuthal flows decreases.

484 The azimuthal charge-averaged ion velocity leads to twisting of the magnetic field, via
485 the magnetic induction equation, in the midplane of the cloud. The resulting twist in the
486 magnetic field then propagates in the field-aligned direction away from the cloud midplane as an
487 Alfvén wave. The magnetic field and ion velocity perturbations are perpendicular to the wave
488 propagation direction and no perturbations were observed in the background ion density or
489 magnetic field strength. It is therefore concluded that the disturbance propagates as a shear
490 Alfvén wave. The energy carried by the shear Alfvén wave is anti-parallel to the magnetic field
491 direction when the magnetic field and ion velocity perturbations are in the same direction, and
492 parallel to the magnetic field direction when the magnetic field and ion velocity perturbations are
493 in the opposite directions [*Siscoe*, 1983]. In the results reported here, the intermediate Alfvén

494 wave speed in the background oxygen ions is $164\ km/s$ which corresponds to the wave
495 traveling 148 km in 0.9 seconds as shown in Figure 7c. Current closure in the shear Alfvén wave
496 is primarily carried by the electrons in the field-aligned direction and by the ions in the
497 perpendicular direction [Gekelman et al., 1997; Gekelman et al., 2011]. An examination of the
498 ion and electron velocities in the model results shows that this is the case here as well.

499

500 **5 Conclusions**

501 The STC model has been developed to study the evolution of artificial clouds in a
502 background ionosphere/thermosphere. The model solves the 3-D multi-fluid MHD continuity
503 and momentum equations for multiple neutral and ion species with the induction equation for the
504 magnetic field, and source terms for photoionization chemistry. The results presented here are
505 consistent with the model results presented by MS93. The neutral barium cloud expands radially
506 with a spherical density distribution. The barium ion cloud, produced by ionization of the
507 neutral barium cloud, expands mostly along the magnetic field lines. Both the barium and
508 oxygen ions are observed to rotate about the magnetic field. Late in the simulation, an oxygen
509 ion density depletion is observed with density enhancements on opposite field-aligned sides of
510 the depletion. Several features are observed that were not reported in MS93 that can be
511 attributed to the addition of the magnetic induction equation. A diamagnetic cavity develops and
512 disappears. Initially there is an oxygen ion density enhancement in the center of the cloud that
513 later evolves into a density depletion. The direction of the ion rotation about the magnetic field
514 alternates with time. The associated magnetic field twist propagates away from the cloud along
515 the field line as a shear Alfvén wave.

516

517 **Acknowledgments**

518 No data sets were directly used in this work. The work of DMO and JMH were supported
519 by the Air Force Office of Scientific Research task “Global Ionospheric Processes” and by the
520 Space Vehicles Directorate of the Air Force Research Laboratory. The work of TSC was
521 performed under the Air Force Research Laboratory contract FA9453-18-C-0020. The work of
522 JVE was performed under the Air Force Research Laboratory contract FA9453-17-F-0001.

Special thanks to David Cooke for many useful conversations and insightful comments. Data generated for this paper is available on the Zenodo data repository (https://zenodo.org/record/4315743)

References

Bernhardt, P. A. (1979). Three-dimensional, time-dependent modeling of neutral gas diffusion in a nonuniform, chemically reactive atmosphere. *Journal of Geophysical Research: Space Physics*, *84*(A3), 793-802, https://doi.org/10.1029/JA084iA03p00793.

Bernhardt, P. A., Roussel-Dupre, R. A., Pongratz, M. B., Haerendel, G., Valenzuela, A., Gurnett, D. A., & Anderson, R. R. (1987). Observations and theory of the AMPTE magnetotail barium releases. Journal of Geophysical Research: Space Physics, 92(A6), 5777-5794, https://doi.org/10.1029/JA092iA06p05777.

Bernhardt, P. A. (1992). Probing the magnetosphere using chemical releases from the Combined Release and Radiation Effects Satellite. Physics of Fluids B: Plasma Physics, 4(7), 2249-2256.

Bernhardt, P. A., C. L. Siefring, S. J. Briczinski, A. Viggiano, R. G. Caton, T. R. Pedersen, J. M. Holmes, S. Ard, N. Shuman, and K. M. Groves (2017), A physics-based model for the ionization of samarium by the MOSC chemical releases in the upper atmosphere, Radio Sci., 52, doi:10.1002/2016RS006078.

Blaunstein, N. S., Milinevsky, G. P., Savchenko, V. A., & Mishin, E. V. (1993). Formation and development of striated structure during plasma cloud evolution in the Earth's ionosphere. Planetary and space science, 41(6), 453-460.

Boris, J. P., & Book, D. L. (1976). Solution of continuity equations by the method of flux-corrected transport. In *Methods in computational physics. Advances in research and applications. Vol. 16*.

Davis, T. N. (1979). Chemical releases in the ionosphere. Reports on Progress in Physics, 42(9), 1565.

Delamere, P. A., Stenbaek-Nielsen, H. C., Hampton, D. L., & Wescott, E. M. (1996). Optical observations of the early (t< 5 s) ion dynamics of the CRRES G1, G9, and G11A releases. Journal of Geophysical Research: Space Physics, 101(A8), 17243-17257, https://doi.org/10.1029/96JA00862.

Eccles, J. V., & Raitt, W. J. (1992). Reactive collision terms for fluid transport theory. *Planetary and space science*, *40*(1), 47-62.

557 Gekelman, W., Vincena, S., Leneman, D., & Maggs, J. (1997). Laboratory experiments on shear
558 Alfvén waves and their relationship to space plasmas. Journal of Geophysical Research:
559 Space Physics, 102(A4), 7225-7236, https://doi.org/10.1029/96JA03683.

560 Gekelman, W., Vincena, S., Van Compernolle, B., Morales, G. J., Maggs, J. E., Pribyl, P., &
561 Carter, T. A. (2011). The many faces of shear Alfvén waves. Physics of Plasmas, 18(5),
562 055501.

563 Haerendel, G., Paschmann, G., Baumjohann, W., & Carlson, C. W. (1986). Dynamics of the
564 AMPTE artificial comet. Nature, 320(6064), 720-723.

565 Haerendel, G. (2019). Experiments with plasmas artificially injected into near-Earth space.
566 Frontiers in Astronomy and Space Sciences, 6, 29.

567 Harnett, E. M., and R. M. Winglee (2006), Three-dimensional multifluid simulations of
568 ionospheric loss at Mars from nominal solar wind conditions to magnetic cloud events, J.
569 Geophys. Res., 111, A09213, doi:10.1029/2006JA011724.

570 Holmes, J. M., Dressler, R. A., Pedersen, T. R., Caton, R. G., & Miller, D. (2017). A combined
571 spectroscopic and plasma chemical kinetic analysis of ionospheric samarium releases.
572 Radio Science, 52(5), 521-538, https://doi.org/10.1002/2016RS006084.

573 Huba, J. D., Bernhardt, P. A., & Lyon, J. G. (1992). Preliminary study of the CRRES
574 magnetospheric barium releases. Journal of Geophysical Research: Space Physics,
575 97(A1), 11-24, https://doi.org/10.1029/91JA02144.

576 Ledvina, S. A., Ma, Y. J., & Kallio, E. (2008). Modeling and simulating flowing plasmas and
577 related phenomena. In *Comparative Aeronomy* (pp. 143-189). Springer, New York, NY.

578 Lühr, H., Southwood, D. J., Klöcker, N., Dunlop, M. W., Mier-Jedrzejowicz, W. A. C.,
579 Rijnbeek, R. P., . & Acuna, M. (1986). In situ magnetic field observations of the AMPTE
580 artificial comet. Nature, 320(6064), 708-711.

581 Lühr, H., Kloecker, N., & Acuña, M. H. (1988). The diamagnetic effect during AMPTE's tail
582 releases: Initial results. Advances in space research, 8(1), 11-14.

583 Ma, T. Z., & Schunk, R. W. (1991). Plasma cloud expansion in the ionosphere: Three-
584 dimensional simulation. Journal of Geophysical Research: Space Physics, 96(A4), 5793-
585 5810, https://doi.org/10.1029/90JA02618.

586 Ma, T. Z., & Schunk, R. W. (1993). Ionization and expansion of barium clouds in the
587 ionosphere. *Journal of Geophysical Research: Space Physics*, *98*(A1), 323-336,
588 https://doi.org/10.1029/92JA01552.

589 Ma, T. Z., & Schunk, R. W. (1994). Dynamics of three-dimensional plasma clouds with coupling
590 to the background ionosphere. Journal of Geophysical Research: Space Physics, 99(A4),
591 6331-6344, https://doi.org/10.1029/93JA02645.

592 MacNamara, S., & Strang, G. (2016). Operator splitting. In Splitting Methods in
593 Communication, Imaging, Science, and Engineering (pp. 95-114). Springer, Cham.

594 Mantina, M., Valero, R., Cramer, C. J., & Truhlar, D. G. (2013). Atomic radii of the elements.
595 *CRC Handbook of Chemistry and Physics*, *94*.

596 Milinevsky, G. P., Kashirin, A. I., Romanovsky, Y. A., Stenbaek-Nielsen, H. C., & Kelley, M. C.
597 (1993). Long-lived artificial ion clouds in the Earth's ionosphere. Geophysical research
598 letters, 20(11), 1019-1022, https://doi.org/10.1029/93GL01348.

599 Miller, T. M. (2000). Atomic and molecular polarizabilities. *CRC Handbook of Chemistry and*
600 *Physics*, *77*, 193-202.

601 Pedersen, T. R., Caton, R. G., Miller, D., Holmes, J. M., Groves, K. M., & Sutton, E. (2017).
602 Empirical modeling of plasma clouds produced by the Metal Oxide Space Clouds
603 experiment. Radio science, 52(5), 578-596, https://doi.org/10.1002/2016RS006079.

604 Press, W. H., Teukolsky, S. A., Flannery, B. P., & Vetterling, W. T. (1992). *Numerical recipes in*
605 *Fortran 77: volume 1, volume 1 of Fortran numerical recipes: the art of scientific*
606 *computing*. Cambridge university press.

607 Rosenberg, N. W. (1971). Observations of striation formation in a barium ion cloud. Journal of
608 Geophysical Research, 76(28), 6856-6864, https://doi.org/10.1029/JA076i028p06856.

609 Schunk, R. W. (1977). Mathematical structure of transport equations for multispecies flows.
610 *Reviews of Geophysics*, *15*(4), 429-445, https://doi.org/10.1029/RG015i004p00429.

611 Schunk, R. W., & Nagy, A. F. (1980). Ionospheres of the terrestrial planets. *Reviews of*
612 *Geophysics*, *18*(4), 813-852, https://doi.org/10.1029/RG018i004p00813.

613 Schunk, R. W., & Szuszczewicz, E. P. (1991). Plasma expansion characteristics of ionized
614 clouds in the ionosphere: Macroscopic formulation. Journal of Geophysical Research:
615 Space Physics, 96(A2), 1337-1349, https://doi.org/10.1029/90JA02345.

616 Siscoe, G. L. (1983). Solar system magnetohydrodynamics. In Solar-terrestrial physics (pp. 11-
617 100). Springer, Dordrecht.

618 Stenbaek-Nielsen, H. C. (1989). Calculated emission rates for barium releases in space.
619 Planetary and space science, 37(11), 1441-1452.

620 Stoffregen, W. (1970). Electron density variation observed in the E-layer below an artificial
621 barium cloud. Journal of Atmospheric and Terrestrial Physics,32(2), 171-177.

622 Strang, G. (1968). On the construction and comparison of difference schemes. *SIAM journal on*
623 *numerical analysis*, *5*(3), 506-517.

624 Szuszczewicz, E. P., Hunton, D. E., Wygant, J. R., & Schunk, R. W. (1993). Observations and
625 model comparisons of early-time expansion characteristics of a satellite-Borne barium-
626 lithium release at F-region altitudes. Geophysical Research Letters,20(19), 2031-2034,
627 https://doi.org/10.1029/93GL01451.

628 Winglee, R. M. (2004), Ion cyclotron and heavy ion effects on reconnection in a global
629 magnetotail, J. Geophys. Res., 109, A09206, doi:10.1029/2004JA010385.

630 Winske, D. (1989). Development of flute modes on expanding plasma clouds. Physics of Fluids
631 B: Plasma Physics, 1(9), 1900-1910.

632 Winske, D., Huba, J. D., Niemann, C., & Le, A. (2019). Recalling and updating research on
633 diamagnetic cavities: experiments, theory, simulations. Frontiers in Astronomy and Space
634 Sciences, 5, 51.

635 Xie, L., Li, L., Wang, J., & Zhang, Y. (2014). Three-dimensional, two-species
636 magnetohydrodynamic studies of the early time behaviors of the Combined Release and
637 Radiation Effects Satellite G2 barium release. Physics of Plasmas, 21(4), 042903.

638 Zalesak, S. T. (1979). Fully multidimensional flux-corrected transport algorithms for fluids.
639 Journal of computational physics, 31(3), 335-362.

640 Zhang, X., Sun, A., Tian, L., & Zhang, G. (2019). Three-dimensional fluid simulations of the Cs
641 plasma release in the ionosphere. AIP Advances, 9(1), 015117.

642

643